Mid-infrared photonic crystal cavities

Master thesis #2
Rick Leijssen

External supervisors
Raji Shankar
Marko Lončar
School of Engineering and Applied Sciences,
Harvard University

LION supervisor
Michiel de Dood
Quantum Optics & Quantum Information,
Universiteit Leiden

March 25, 2012

Contents

1 Introduction **2**
1.1 Mid-infrared photonics 2
1.2 Photonic crystal cavities 3
1.3 Resonant scattering characterisation 3

2 Mid-infrared photonic crystal cavities in silicon **6**
2.1 Introduction 6
2.2 Design 7
2.3 Fabrication 8
2.4 Characterization 9
2.5 Conclusion 14

3 Optical bistability **15**
3.1 Introduction 15
3.2 Experiments 15
3.3 Discussion 16
3.4 Conclusion 20

4 Gas sensing **21**
4.1 Introduction 21
4.2 Detection limit 22
4.3 Experimental 22
4.4 Conclusion 26

A Temporal coupled mode theory **28**

B Nonlinear resonance shift **30**

Chapter 1

Introduction

This thesis describes the results of a six-month project I performed in the group of Prof. Marko Lončar at Harvard University. In this project I collaborated closely with Raji Shankar and Dr. Irfan Bulu.

This thesis is structured as follows. Chapter 1 introduces a few key concepts. Chapter 2 contains the main results of the project as reported in the paper *Mid-infrared photonic crystal cavities in silicon*, published in Optics Express in March 2011[1]. Chapter 3 describes experiments on optical bistability, and chapter 4 describes preliminary tests of a gas sensing scheme.

My involvement in this project started shortly after the realisation and partial characterisation of several working devices. My work therefore mainly concerned the further characterisation of these devices, as well as improving and expanding the characterisation setup. The improvements to the setup include the scanning system described in section 2.4 and the gas flow system described in section 4.3.

1.1 Mid-infrared photonics

The field of mid-infrared photonics operates roughly in the wavelength range of 2–20 µm. The field of near-infrared photonics, operating at the 'telecom' wavelength at 1.5 µm, has received a lot of attention due to the availability of coherent light sources and detectors. In the mid-infrared wavelength range, high-power sources and sensitive detectors have only recently become available. This means a lot less work has been done on creating 'passive elements' such as waveguides, resonators, splitters, and couplers than in the near-infrared wavelength range. However, there are a few promising applications in the mid-infrared region that are not possible in the near-infrared:

Free-space communication There are two atmospheric 'windows', wavelength ranges where air is transparent, in the mid-infrared wavelength range: 3–5 µm and 8–14 µm. Optical free-space communication is a promising high-bandwidth application, and the mid-infrared region has the advantage of lower scattering over the near-infrared wavelength range[2].

Trace gas sensing Several gases important in environmental, safety, or health monitoring show absorption bands in the mid-infrared wavelength region.

Because of the specific characteristics of these absorption bands, which are different for each molecule, the mid-infrared region is also known as the 'fingerprint region'. Mid-infrared photonic devices could be used to create miniaturised sensitive detectors for these gases[3].

High-power nonlinear optics devices in silicon In the near-infrared region, silicon exhibits absorption at high operating powers because of two-photon absorption. Using silicon in mid-infrared devices has the potential to allow very high pumping powers without significant absorption, which might lead to nonlinear optical devices in silicon[4, 5].

To be able to create devices for use in these applications, we need the elements that can be combined to eventually create integrated optical chips that can serve in these functions. The first steps for that are to create waveguides and resonators. Optical resonators can be made very compact using photonic crystal cavities, since they enable us to trap light in a very small volume, comparable to the size of the wavelength of the light.

1.2 Photonic crystal cavities

Photonic crystals are devices with a periodic variation in refractive index on a length scale that is comparable to the wavelength of light[6]. The varying refractive index modifies propagating electromagnetic waves in a similar way that the periodicity of semiconductor crystals modifies electron motion. The Bragg scattering from the periodic structure gives rise to allowed modes and, in some cases, forbidden bands where no modes exist. The creation of such a photonic band gap in two dimensions can be achieved with a hexagonal lattice, such as the one shown in figure 1.1. In order to create a full photonic bandgap in 3 dimensions, a 3-dimensional photonic crystal is needed, but these are notoriously hard to fabricate. Instead, a (2-dimensional) photonic crystal slab structure provides confinement in the vertical direction by total internal reflection.

If a defect is created in such a photonic crystal slab with a photonic band gap, the defect region will allow modes in the band gap. These modes will be confined to the defect region in the vertical direction by the index contrast of the slab with the surrounding air, and in the in-plane direction by Bragg scattering from the photonic crystal structure. In this project we used the so-called L3 photonic crystal cavity, which consists of removing three adjacent holes in a hexagonal lattice of air holes to form a line defect supporting a linearly polarized mode[7]. The design is further discussed in section 2.2 and can be seen in figure 2.1.

1.3 Resonant scattering characterisation

For free-space characterisation of photonic crystal cavities we use the resonant scattering method[8, 9]. Fig. 1.2 shows a diagram explaining the principle behind the technique. Since only a small fraction of the light incident on the cavity couples to the resonant mode and is emitted again towards the detector, the direct reflection or transmission from the cavity dominates the detected signal. In order to separate the direct and resonant contributions to this signal, the light is cross-polarized to suppress the direct contribution. If the cavity is oriented

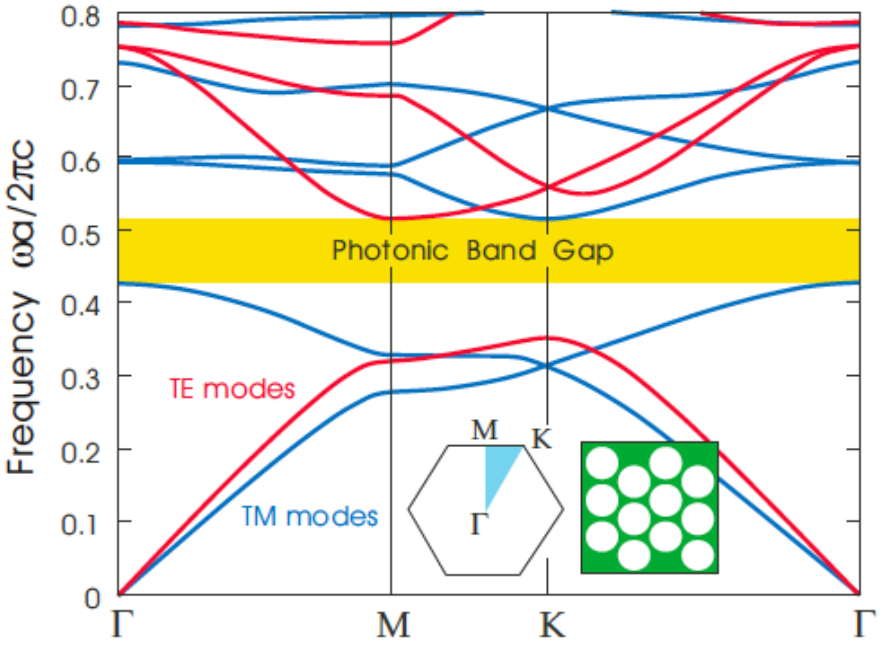

Figure 1.1: Illustration of the photonic band structure of an infinite 2-dimensional hexagonal lattice of air holes in a high-index material[6].

at 45 degrees with respect to both the input and output polarizers, light will still resonantly couple to the cavity, albeit less so because of the polarization mismatch. However, since the emitted light is polarized in the direction corresponding to the orientation of the device, half of the emitted light is transmitted by the output polarizer. This results in a vastly improved signal-to-background ratio.

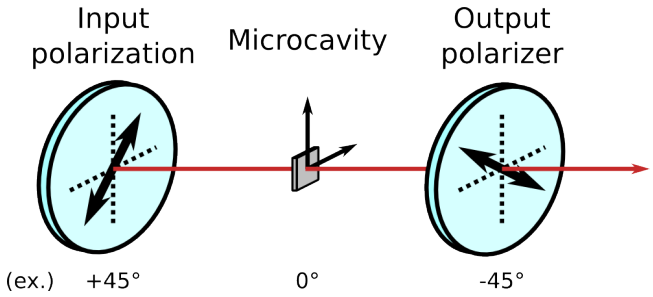

Figure 1.2: Diagram explaining the resonant scattering characterisation scheme[9]. By detecting the light from the microcavity in cross-polarization most of the direct reflection or transmission is suppressed. If the microcavity is positioned at 45 degrees with respect to the input and output polarizers light will resonantly couple to the microcavity and be emitted with the polarization corresponding to the orientation of the microcavity, ensuring that a large part of this emitted light can reach the detector.

Chapter 2

Mid-infrared photonic crystal cavities in silicon

As published in Optics Express, March 2011[1].

Raji Shankar[1] Rick Leijssen[1 2] Irfan Bulu[1] Marko Lončar[1]

abstract We demonstrate the design, fabrication, and characterization of silicon photonic crystal cavities realized in a silicon on insulator (SOI) platform, operating at a wavelength of 4.4 µm with a quality factor of 13,600. Cavity modes are imaged using the technique of scanning resonant scattering microscopy. To the best of our knowledge, this is the first demonstration of photonic devices fabricated in SOI and operating in the 4-5 µm wavelength range.

2.1 Introduction

The mid-infrared (IR) wavelength range (2-20 µm) has recently become more accessible due to the development of high-power, room-temperature operational sources and sensitive detectors. At the same time, little work has been done in developing passive photonic elements such as waveguides, resonators, splitters, etc. for the mid-IR. However, integrated photonics at this wavelength range would be useful for a variety of applications for which the mid-IR is particularly suited, including thermal imaging, biological sensing, chemical bond spectroscopy, free space communications and trace gas sensing.

Conventionally, mid-IR photonics is associated with the III-IV materials used for active optoelectronic devices (lasers and detectors), as well as chalcogenide glasses used for passive photonic elements[10]. However, it has recently been proposed by R. Soref that silicon is also a promising material for the mid-IR, as it exhibits low loss throughout much of the mid-IR[5, 11]. Using silicon as the material of choice for the mid-IR would allow us to take advantage of well-developed fabrication techniques and CMOS compatibility, making the realization of on-chip integrated mid-IR devices more realistic. Finally,

[1]School of Engineering and Applied Sciences, Harvard University, Cambridge, MA 02138, USA

[2]Huygens Laboratory, Leiden University, P.O. Box 9504, 2300 RA Leiden, The Netherlands

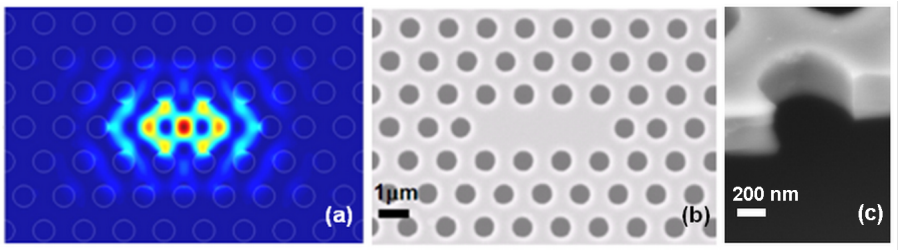

Figure 2.1: (a) Mode profile of E_z field component of L3 photonic crystal cavity with $a = 1.34$ μm, $r = 0.263a$, $t = 0.5$ μm, and hole shift $s = 0.15a$, with resonance wavelength of 4.604 μm and Q factor of 24,000. (b) Scanning electron micrograph of fabricated L3 photonic crystal cavity. (c) Scanning electron micrograph of etched sidewall of photonic crystal cavity hole; image is taken at 45° tilt.

due to the lack of two- and three-photon absorption in the mid-IR, the power density of optical signals propagating in Si waveguides or stored in Si optical cavities can be significantly higher than at the near-IR wavelengths used for telecommunications[12, 4, 13, 14]. Therefore, Si-based on-chip optical networks operating in mid-IR may find applications as optical interconnects for datacom. Silicon-on-sapphire waveguides[15] and ring resonators[16] have already been demonstrated in the past year. In this work, we demonstrate the first wavelength-scale optical resonators, in the form of L3 photonic crystal cavities[7], in the CMOS compatible silicon-on-insulator material platform. High quality factor (Q) and low mode volume optical resonators in the mid-IR are of interest for many applications including trace gas sensing, optical interconnects, and so on.

2.2 Design

We chose the well-known L3 cavity design[7] for our photonic crystal cavities due to the relative ease of free-space in- and out-coupling in this cavity (Fig. 2.1). This cavity design consists of a two-dimensional hexagonal photonic crystal lattice of air holes in a Si slab, with three central air holes removed to form a line defect. Bragg scattering accounts for electromagnetic confinement in the x and y directions, while index contrast provides confinement in the z direction. The cavity mode is linearly polarized. To further achieve confinement of the light to the cavity region, the air holes on either side of the cavity are shifted outwards, decreasing the phase mismatch between the cavity region and the Bragg mirror region formed by the photonic crystal (Fig. 2.1a). This allows for higher quality (Q) factors to be achieved[7].

The cavities were designed using three-dimensional finite-difference time-domain method (Lumerical Solutions, Inc.) for a Si device layer thickness t of 500 nm. The periodicity of the photonic crystal lattice is $a = 1.34$ μm, and the air hole radius $r = 353$ nm ($r/a = 0.263$). The air hole shift s was scanned from zero shift to a maximum shift of $0.275a$ in order to optimize the Q factor of the cavity. An air hole shift of $s = 0.2a$ results in an optimal design at $\lambda = 4.615$ μm with a Q factor of 66,000 when 10 mirror pairs surround the cavity region. The mode profile is plotted in Fig. 2.1a, and the theoretical calculations for the

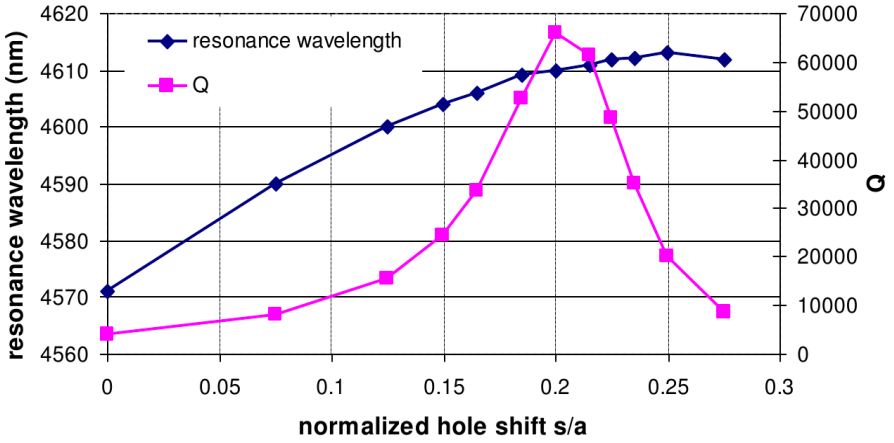

Figure 2.2: Results of FDTD calculations showing L3 photonic crystal cavity resonance wavelengths and quality factors as a function of s, the hole shift.

resonance wavelength and Q factor as a function of s are shown in Fig. 2.2. As expected, as the hole shift is increased, the cavity resonance is pushed to longer wavelengths, due to the increase in high-dielectric material in the cavity region.

2.3 Fabrication

The devices were fabricated on a silicon-on-insulator (SOI) substrate (SOITEC Inc.), with a device layer thickness of 500 nm and SiO_2 layer thickness of 3 µm. ZEP (Zeon Corp), a positive electron-beam resist, was used as a mask for electron-beam lithography. The film was deposited by spinning pure ZEP onto the substrate at a rate of 2000 rpm, followed by a post-spin bake at 180 °C for 3 minutes, resulting in a film thickness of 550 nm. A standard 100 kV electron beam lithography tool (Elionix ELS-7000) was used to define patterns in the ZEP layer, which were then developed in o-xylene for 40 seconds followed by a rinse in isopropanol alcohol. Etching was performed in a reactive ion etcher (STS-ICP-RIE) using C_4F_8, SF_6, and H_2 gases in a two step process. The first step was a Si etch step at 10 mTorr with a C_4F_8 flow rate of 130 sccm, a SF_6 flow rate of 80 sccm, and no H_2 flow. The second step was a Si and SiO_2 etch step at 20 mTorr with a C_4F_8 flow rate of 130 sccm, SF_6 flow rate of 80 sccm, and a H_2 flow rate of 15 sccm. The devices were undercut using a 7:1 buffered oxide etch for 45 minutes. A scanning electron micrograph of a completed device is shown in Fig. 2.1b. A number of different L3 photonic crystal cavities were fabricated by varying the air hole shift, resulting in cavities with different quality factors and resonance wavelengths as described earlier. Sets of cavity with both four mirror hole pairs and ten mirror hole pairs were fabricated.

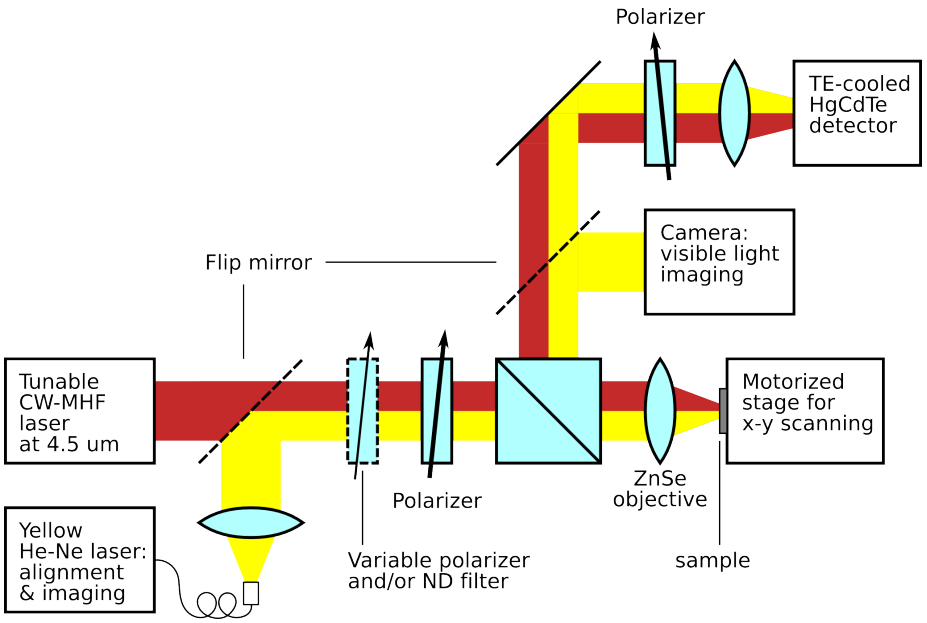

Figure 2.3: Schematic of experimental setup used for resonant scattering-based characterization of photonic crystal cavities.

2.4 Characterization

We used the resonant scattering method[8, 9] to test our cavities (Fig. 2.3). Light from a tunable quantum cascade laser (QCL) with emission from 4.315 to 4.615 µm (Daylight Solutions, Inc.) is sent into a ZnSe objective lens with numerical aperture (NA) of 0.22 and focused onto the sample, which is placed so that the cavity mode polarization is oriented at 45 degrees with respect to the E-field of the laser spot. Since the QCL emission is invisible, a yellow HeNe laser beam was aligned to the path of the QCL and then used to align the rest of the optics. A Ge neutral density filter with optical density of 1.0 is used to reduce the light intensity. The sample is mounted on an automatic micropositioner stage, which can be scanned using computer control. The light that is coupled and re-emitted by the photonic crystal cavities is backscattered into the ZnSe objective, and then travels through a second polarizer (the analyzer) which is cross-polarized with respect to the input polarizer, before being focused onto a thermoelectrically cooled mercury cadmium telluride (MCT) detector. This cross-polarization method enhances the signal-to-background ratio of the resonantly scattered light (the signal) to the non-resonantly scattered light (the background). Depending on this ratio, the resonance peak can appear as a Lorentzian or a Fano lineshape caused by the phase shift between the resonant (re-emitted by cavity) and non-resonant components of the back-scattered signal[17].

The experimental results for photonic crystal cavities with 10 mirror hole pairs are shown in Fig. 2.4. Photonic crystal cavity modes are found within the range of 4.38 to 4.42 um. As predicted by theory (Fig. 2.2), the cavity resonance wavelengths redshift as the air hole shift s is increased from zero to a maximum

of $s = 0.225a$ (Fig. 2.4b). The Q-factors also roughly follow the trend predicted by theory. A peak Q-factor of 13,600 is found for $s = 0.15a$, representing the highest Q factor measured for any Si-based optical cavity in the mid-infrared (Fig. 2.4b). The inset in Figure 2.4a shows the measured Fano lineshape of the resonance along with the theoretical fit $F(f)$[17] given by:

$$F(f) = A_0 + F_0 \frac{[q + 2(f - f_0)/\Gamma]^2}{1 + [2(f - f_0)/\Gamma]^2} \tag{2.1}$$

where A_0 and F_0 are constants, q is the Fano parameter, f_0 is the cavity mode frequency, and Γ is the linewidth. The fit is plotted in terms of the wavelength $\lambda = c/f$, where c is the velocity of light. We extract the quality factor from the ratio of f_0 to Γ. In the case of the $s = 0.15a$ cavity, the extracted linewidth was 5.0 GHz with a f_0 of 68 THz. In the $s = 0.2a$ cavity we did not detect a resonance, possibly due to the low NA (0.22) of the ZnSe objective used to collect light. With a low NA lens, it is difficult to couple light into and collect light from higher-Q cavities, where the cavity emission is largely at angles outside the collection cone of the lens[8]. This is also the reason why the resonance for $s = 0.225a$ (magenta in Figure 2.4a) has a poor signal-to-noise ratio. Part of the challenge of working in the mid-IR is the paucity of high-quality optical components, such as high numerical aperture objective lenses, more readily available at other wavelength regimes. This also results in a large focal spot size, approximately 20 µm in diameter. In order to improve signal-to-noise ratio in our experiments, we could increase the excitation power of our laser. However, when the QCL output power was increased to 100 mW (only about 3-5 % of this power gets coupled into the cavity), we noticed the evidence of optical bistability in our photonic crystal cavities[18]. We believe the origin of this nonlinear effect is thermo-optic in nature, and is most likely due to the finite linear absorption of Si in the mid-infrared[11]. We are exploring this bistability for future work.

In order to further confirm that the observed resonances are indeed associated with cavity modes, it is important to visualize their spatial profiles. However, since no true viewer cards exist for the mid-IR wavelength range, and mid-IR cameras are rather expensive, we adapted the scanning-confocal microscopy approach to image our devices[19]. We call this method scanning resonant scattering microscopy. A single mid-IR detector is used, and the spatial profile is obtained by scanning the sample in x- and y-direction using computer-controlled micropositioners. In order to locate the cavities, we scan the sample stage in both x- and y- directions at an arbitrary wavelength. The outlines of the cavities can be made out at all wavelengths, so we can then move to the center of the photonic crystal cavity region and sweep the laser in wavelength in order to obtain a resonant scattering spectrum. This procedure allows us to precisely position the laser beam onto our cavities. Furthermore, we can obtain the image of the cavity resonance by tuning the laser to the cavity resonance and moving the sample holder stages in the x- and y-directions and recording the detector reading at each position. Images obtained using this approach are shown in Figure 2.5. It can be seen that the cavity regions light up at the wavelengths corresponding to the resonance peak in the wavelength scan, and remain dark off-resonance, confirming that the peaks we see in the wavelength scans do indeed correspond to L3 photonic crystal cavity modes. In effect, this imaging approach can be seen as a single-pixel mid-infrared camera, allowing

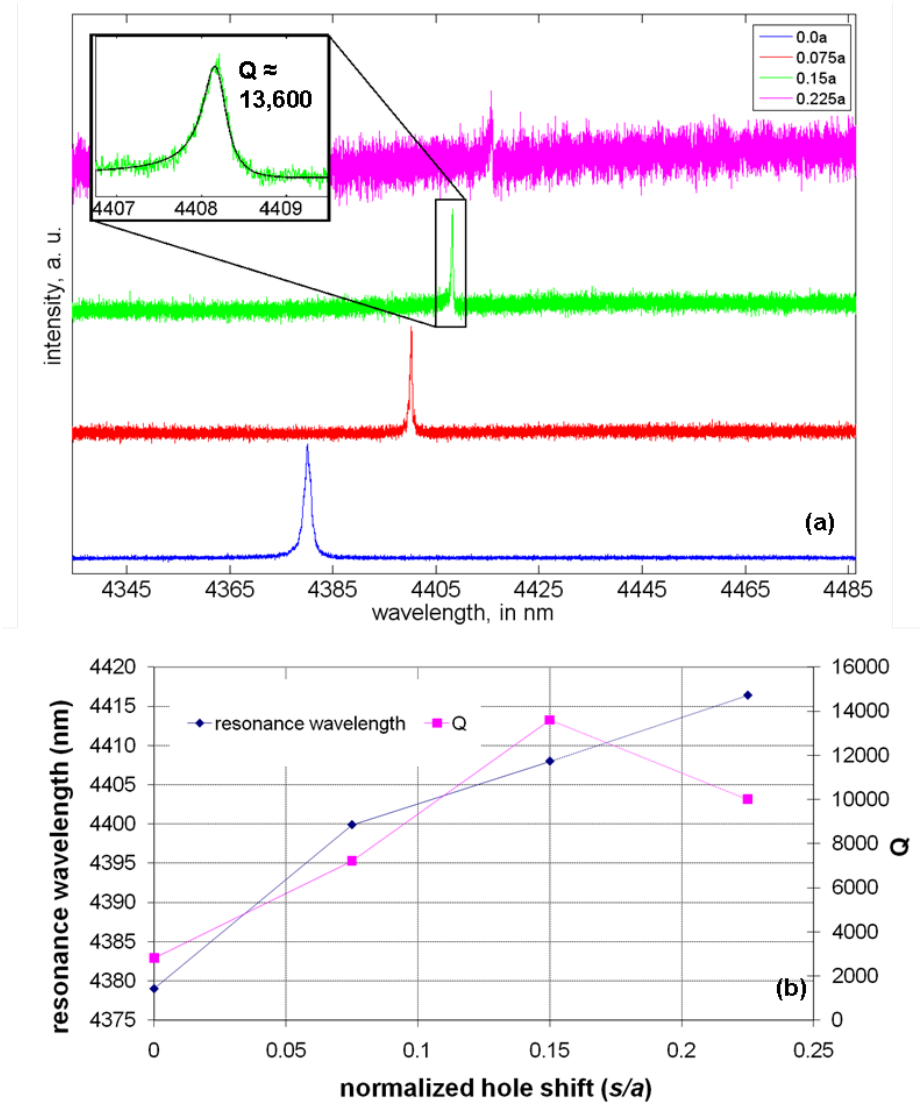

Figure 2.4: (a) Resonant scattering spectra of photonic crystal cavities with $s = 0$, $s = 0.075a, s = 0.15a, s = 0.225a$. Scale is linear. Inset shows Fano fit to $s = 0.15a$ cavity. Fitting parameters are $A_0 = 5.6\text{e-}5$, $q = 2.52$, $\Gamma = 5.0$ GHz, $f_0 = 68$ THz, and $F_0 = 0.0013$. Cavity with $s = 0.2a$ did not show a resonance. (b) Resonance wavelength and Q vs. s for measured cavities. A peak Q of 13,600 is measured at 4408 nm. Lines between points are there to guide the eye.

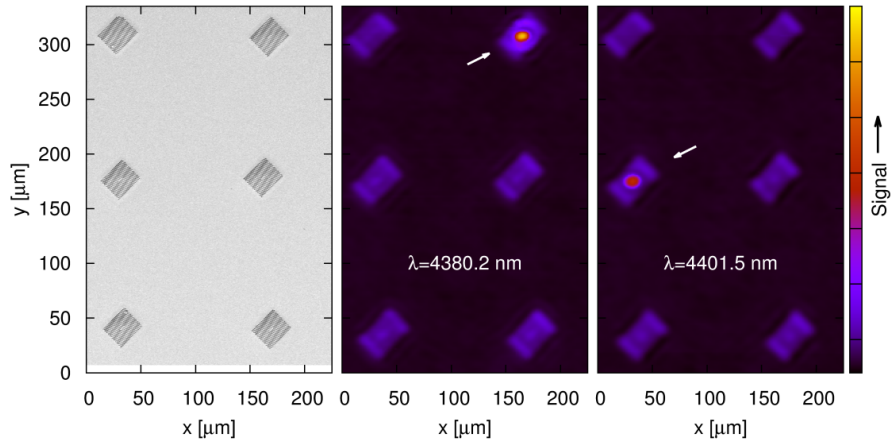

Figure 2.5: Mid-infrared scanning resonant scattering image of an array of 5 cavities (upper left hand structure is photonic crystal with no cavity). Scanning electron micrograph is provided for comparison. When our laser is tuned to one of the cavity resonances, and scanned over the cavity array, only the cavity in resonance with the laser lights up. For example, when 4380.2 nm light, corresponding to the resonance of the top right cavity in the center panel, is scanned over the array, only that cavity appears "ON", featuring a bright spot in its center. Alternatively, when laser is tuned to 4401.5 nm and scanned over the array, only the middle-left cavity (rightmost panel) resonates.

for the visualization of fabricated structures and resonant modes without the use of extremely expensive mid-IR cameras that are commercially available.

In Figure 2.6, we show a spectrum and scanning mid-IR images of additional resonances that were observed in our four-mirror hole pair devices. These devices were placed relatively close together, with a separation of 22 µm in the y-direction. Resonant scattering spectra of these cavity devices show two extra peaks appearing (at 4.433 µm and 4.567 µm) in addition to the cavity resonance peak (4.444 µm). Using our scanning resonant scattering microscopy technique, we were able to image these modes and attribute them to the inter-cavity resonances of the Fabry-Perot cavity formed between two adjacent photonic crystal structures (Fig. 2.6b): one resonance has an anti-node (leftmost panel, 4.433 µm) and the other one has a node (rightmost panel, 4.567 µm) in the center of the inter-cavity region. The resonance at 4.444 µm (center panel in Fig. 2.6b) corresponds to a bonafide resonance of L3 photonic crystal cavity.

The ability to accurately image the spatial profile of resonances observed in the collected spectra, and therefore unambiguously attribute them to the modes of different cavities, is an important demonstration of the utility of the mid-IR scanning resonant scattering microscopy that we developed. The combination of scanning microscopy and resonant scattering wavelength measurements results in a very powerful tool that overcomes many of the difficulties inherent in working at the mid-IR. Iterating between scanning microscopy and wavelength scanning allows us to optimize our resonant scattering spectra signals more quickly and accurately than we would be able to with only a CCD camera sensitive to visible wavelengths to guide us as to the location of our cavities.

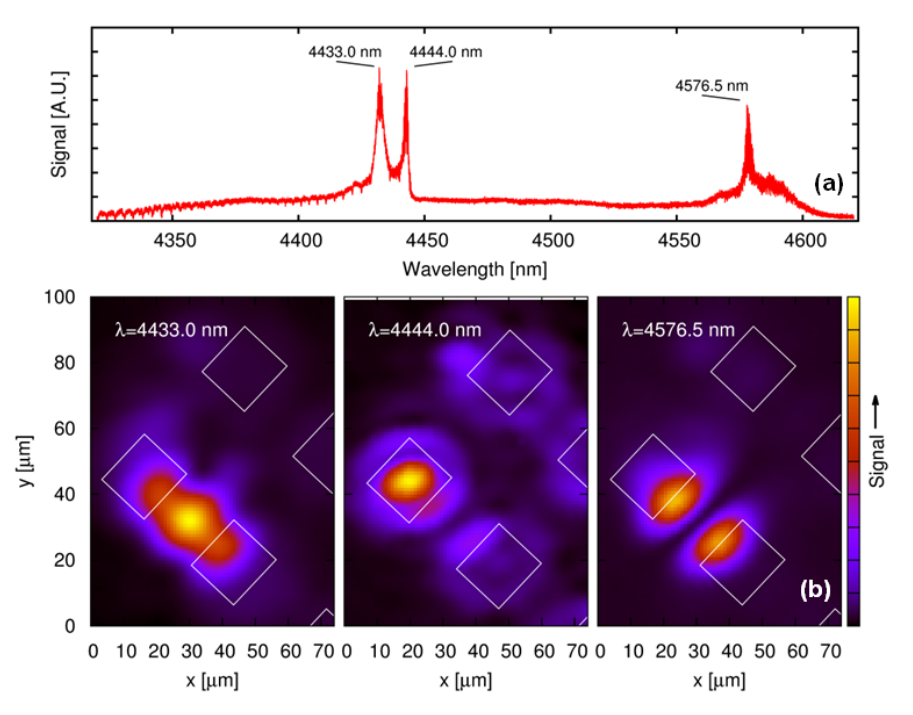

Figure 2.6: (a) Resonant scattering spectrum showing peaks corresponding to two inter-cavity Fabry-Perot resonances (4430.0 nm and 4567.5 nm) and one L3 photonic crystal cavity resonance (4444.0 nm). (b) Scanning images of Fabry-Perot resonances (leftmost and rightmost panels) and photonic crystal cavity resonance (center panel).

We see scanning resonant scattering microscopy as an essential tool in a mid-IR toolbox.

2.5 Conclusion

In conclusion, we have demonstrated the design, fabrication, and characterization of silicon-based photonic crystal cavities for the mid-infrared, with a peak quality factor of 13,600. In addition, we have transferred experimental techniques used at telecommunication and visible wavelengths, most notably resonant scattering and scanning confocal microscopy, to characterize our mid-IR cavities. Further work will be focused on achieving higher quality factor cavities and in coupling mid-IR photonic crystal cavities to waveguides so that the vision of on-chip integrated photonics in the mid-infrared can be attained. Such a fully integrated platform would enable realization of chip-scale systems for trace gas sensing, optical-wireless, on-chip optical interconnects, phased-arrays for LIDAR applications, and so on.

Acknowledgments

The authors would like to thank Leonard Kogos for his help with the experimental setup, and Qimin Quan for many helpful discussions. This work is supported in part by the NSF CAREER grant (ECCS-0846684) and generous support from Schlumberger-Doll Research Center (Cambridge, MA). Device fabrication was performed at the Center for Nanoscale Systems at Harvard University. R. S. would like to thank the NSF GRFP.

Chapter 3

Optical bistability

3.1 Introduction

Optical bistability is a phenomenon that occurs in many nonlinear (optical) systems with feedback[20]. In such systems, hysteresis loops can occur in the ratio of outgoing and ingoing power (P_{out} and P_{in}), like the one shown schematically in figure 3.1. In ref. [20], a simple analytical model is derived for a system that is very similar to ours (see also the almost identical treatment in the Joannopoulos book[6], pp. 214–218). The incoming power in the cavity is dependent on the wavelength difference between the pump light and the cavity resonance wavelength, and the outgoing power is linearly dependent on the energy stored in the cavity. If the cavity resonance wavelength is dependent on the energy stored in the cavity, feedback can occur when the pump power is slightly detuned from the resonance wavelength. The analytical model, obtained with perturbation theory, shows a third-order dependence of the incoming power on the outgoing power, which can then produce a hysteresis loop like the one in figure 3.1.

Optical bistability has been studied in detail in near-infrared photonic crystal cavities, for instance to create an optical switch[18]. Easy ways to study aspects of the bistability include measuring the ratio of outgoing to incoming power to find a hysteresis loop like figure 3.1, and measuring the intensity dependence of transmission or reflection spectra of the device. The latter can show distorted shapes of the resonance peak at high powers, when the cavity is brought into the 'loaded' state while sweeping the laser, shifting its resonance. Positive feedback can then ensure the cavity stays loaded until the laser detuning becomes so large that this is no longer sustainable, and the cavity abruptly switches to the 'empty' state. The characteristic time of the system and the amount of energy required for switching are also important parameters when characterising a bistable system.

3.2 Experiments

Figure 3.2 shows the spectra for the same set of cavities as shown in figure 2.4, but taken at higher power. These spectra were taken at the maximum power output of the laser and without attenuation, which corresponds to about 24 mW of power incident at the cavity. Of this power, 5–10 % is coupled to the cavity.

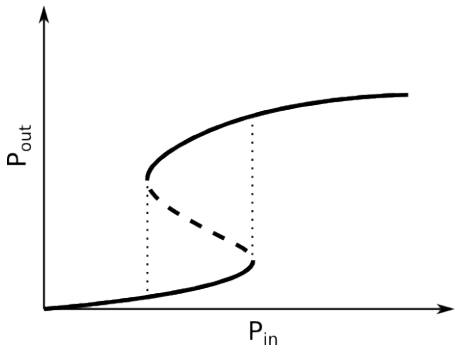

Figure 3.1: Schematic representation of a hysteresis loop in the ratio of outgoing to incoming power (P_{out} and P_{in}). In the dashed part of the curve, the analytical solution in unstable so it is not observable. The dotted lines mark the transition points where the system switches from the 'empty' to the 'loaded' state or vice versa.

The spectra clearly show a drop in the resonantly scattered signal, as the laser is swept from shorter to longer wavelengths. This shape could indicate bistability in the cavity, where incident light of certain frequencies can have two different output intensities, based on which state the cavity is in. The sharp drop would then correspond to when the cavity switches from one state to the other due to the changing frequency of the incident light. In this case, the cavity resonance would have to be redshifted at higher input powers to create the feedback.

More evidence for a bistable effect in the cavity is given in figure 3.3, where the spectrum cavity labeled $0.15a$ in figure 3.2 is shown taken with different input powers incident on the cavity. The power incident on the cavity was varied by turning a variable polarizer placed between the laser and the input polarizer. We calibrated the actual incident power by placing a thermal power meter head behind the ZnSe objective instead of a sample. The threshold for a bistable edge to appear is at an incident power of about 2 mW. At powers slightly below 2 mW the spectrum still doesn't have the expected Lorentzian shape (compare ref. [18] for a better look at the lineshape behaviour in this low-power regime in an optically bistable photonic crystal cavity).

Confirmation of bistability in the cavity can be found in figure 3.4, which shows the resonantly scattered output power of the cavities as a function of the power incident on the cavity, for different detuning from the cavity resonance wavelength. The detunings above 350 pm clearly show a hysteresis loop. As in figure 3.3, bistable operation occurs above about 2 mW of incident power.

3.3 Discussion

In order to estimate the bistability threshold in terms of power coupled into the cavity, we calibrated our detector using the thermal power meter and obtained an estimate for the transfer function of the setup between the sample and the detector by placing a mirror on the sample holder. This way we can estimate the power coupled out of the cavity from the detector readings. Then, since we measured the total Q for the cavities at low power as reported in section 2.4, we can find the coupling Q from temporal coupled mode theory[6]. From the

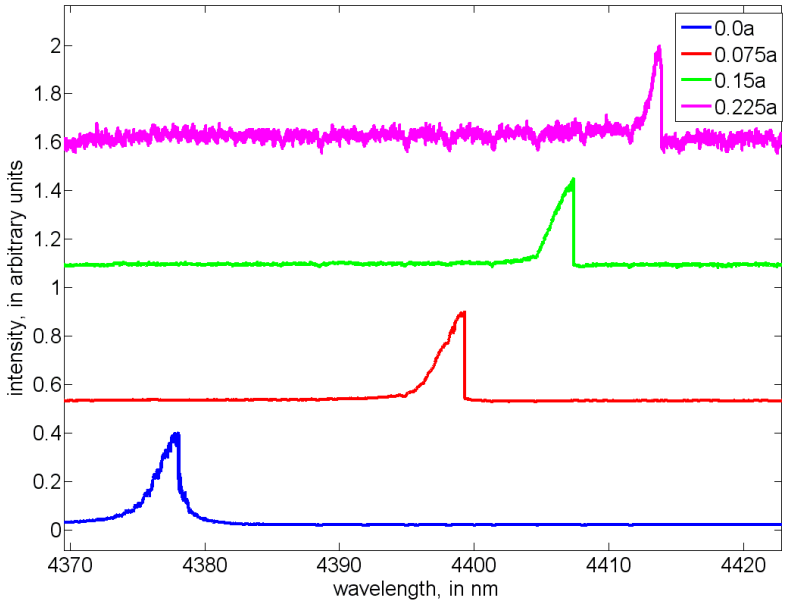

Figure 3.2: Resonant scattering spectra taken of photonic crystal cavities (same as in Fig. 2.4) at a QCL output power of 100 mW, corresponding to about 24 mW of incident power on the cavities. Note the lineshape of the cavity resonances, showing a sudden intensity drop that could indicate optical bistability.

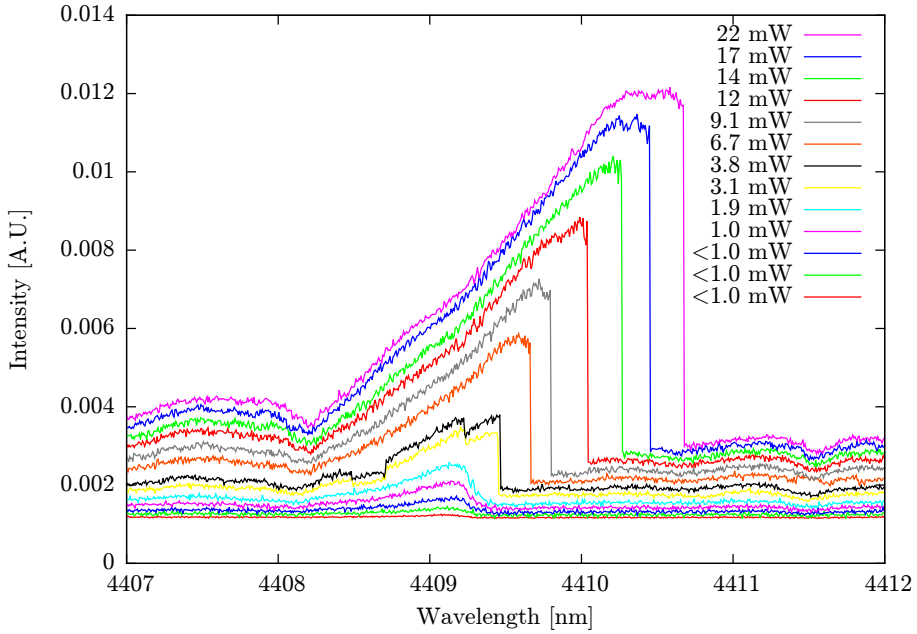

Figure 3.3: Intensity-dependent resonant scattering spectra of the cavity labeled $0.15a$ in figure 3.2. The spectra were taken with the laser sweeping from shorter to longer wavelengths. Above about 2 mW of incident power, a vertical edge is seen in the spectrum.

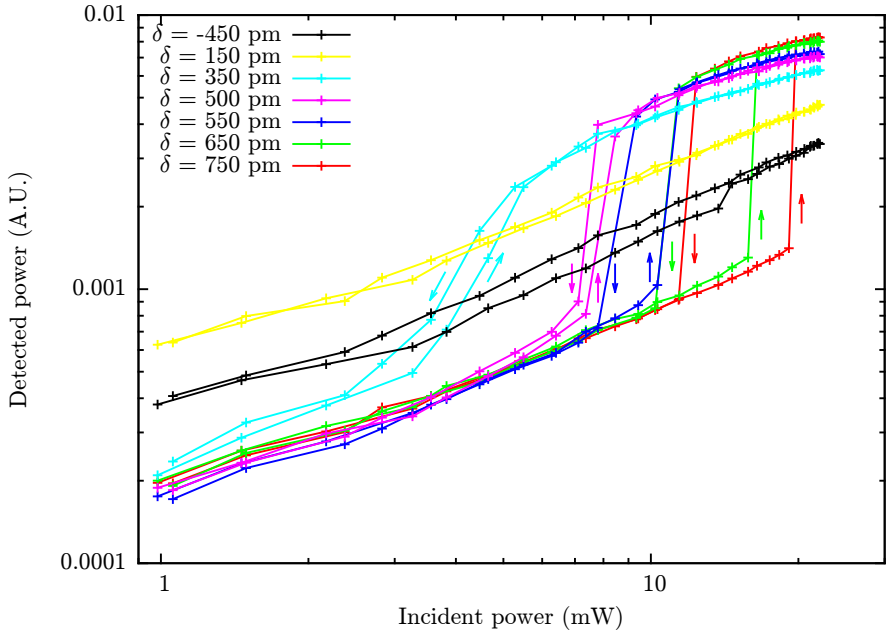

Figure 3.4: Output power versus input power for the cavity of which the spectrum is depicted in figure 3.3, at various detuning (δ) values. The sweep direction of the incident power is indicated with arrows.

temporal coupled mode equations we derive this formula (see appendix A):

$$P_{out} = 4\left(\frac{Q_{total}}{Q_{coupling}}\right)^2 P_{in} \tag{3.1}$$

Using this formula, we find a $Q_{coupling}$ of about 220,000 for the cavity with a Q_{total} of 13,600. This means the coupling efficiency is $Q_{total}/Q_{coupling} \approx 6\%$. At higher powers, the peak is broadened, indicating a lower Q_{total}. Assuming the $Q_{coupling}$ stays roughly the same, this means the relative amount of power coupled into the cavity decreases. In summary, a first (over)estimate for the bistability threshold of this cavity is 6 % of 2 mW, or 120 µW.

Measurement of the intensity-dependent resonant scattering spectra for 2 different cavities like the measurement shown in figure 3.3 gave us the (maximum) wavelength shift versus the incident power of the two cavities, shown in figure 3.5. Together with the previously measured Q_{total} and $Q_{coupling}$ at low power, this can help us find the mechanism for the nonlinear behaviour of the cavity.

Possible mechanisms for the nonlinear behaviour of the cavity are any mechanisms that change the effective refractive index of the cavity as a function of the intensity of the light in the cavity, such as[21, 22]:

Thermo-optic Due to some kind of absorption, the temperature of the cavity changes, causing both a refractive index change and a change in cavity geometry due to thermal expansion of the cavity membrane. Possible absorption mechanisms include linear absorption, multi-photon absorption,

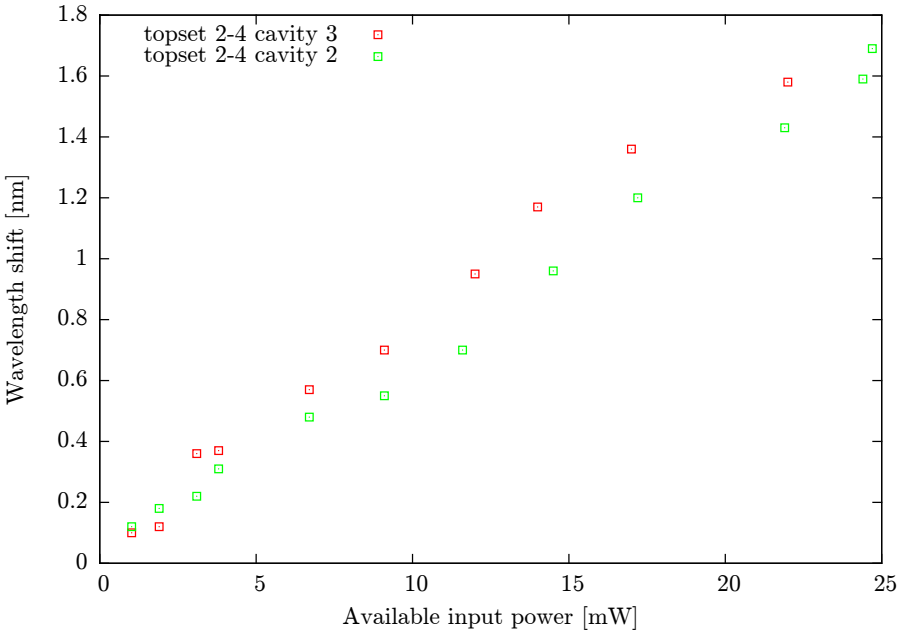

Figure 3.5: Shift of the peak wavelength of 2 different cavity resonances versus the available input power.

or absorption by SiO_2 at the edges of the undercut and in oxide layers on the surface of the silicon.

Kerr effect The electric field of the light directly causes a refractive index change, parametrized by the nonlinear index n_2.

Plasma effect Free carriers, generated by multi-photon absorption change the electrical (and consequently optical) properties of the silicon. Note that this should lead to a lower refractive index, or a blueshift of the cavity resonance. The generated free carriers also cause more absorption, leading to a stronger thermo-optic effect.

Multi-photon induced effects are extremely unlikely at this wavelength: to excite a single electron across the bandgap of silicon, the energy of at least 4 photons is needed. Moreover, if a multi-photon effect was the dominant contribution to the nonlinear effect, this would show up as a nonlinear dependence on input power in figure 3.5. Since the figure shows a linear dependence, multi-photon absorption and the associated free carriers necessary for the plasma effect do not contribute significantly.

Large amounts of SiO_2 are also not expected to be present, since the undercut should have taken care of that. Our spot size is slightly smaller than the cavity membrane, so if the beam is aligned to the middle of the cavity only the layers of native oxide that form on the silicon surface from exposure to air can contribute to the absorption. To be sure the quality of the undercut was not the problem, we gave the cavity another HF treatment, but there was only a small change in the behaviour of the cavities. This change could be caused by a thin layer

of native oxide of the cavities, which was removed by the HF treatment (see figure 4.5 and surrounding discussion for an impression of the effect the oxide layer was having).

This leaves Kerr effect nonlinearity and thermal effects due to linear absorption. We can estimate their effects from literature values of the material properties of the silicon as well as some simple modelling to estimate the thermal resistance of the cavity membrane, as shown in appendix B. The results of this indicate that the effect is most likely caused by linear-absorption induced heating, while Kerr effect nonlinearity does not contribute significantly unless the n_2 of silicon changes dramatically beyond a wavelength of 3 µm. While no direct measurements of the n_2 of silicon in this wavelength region were found in the literature, Miller's rule implies that the dispersion of n_2 is small and linked to the dispersion of the linear refractive index[23, 24], which is small in this wavelength range[25]. Time-domain measurements would be the easiest way to conclusively distinguish between these effects, since thermal effects occur on a much slower timescale than electro-optic effects such as the Kerr effect.

3.4 Conclusion

We observed optical bistability in our mid-infrared photonic crystal cavities. The mechanism causing this is most likely thermal, due to linear absorption in the silicon.

To characterise the linear behaviour of these cavities a low input power is needed, in order to avoid the nonlinear effects. Because of this, the signal-to-noise ratio is lowered. To raise the nonlinear power threshold, cavities with a lower thermal resistance are desirable. A possible solution would be to switch to the silicon-on-sapphire material platform, where the silicon membrane is still attached to the sapphire underneath, which results in a much lower thermal resistance than the air-bridged devices we used in this project[11, 15, 16]. Alternatively, waveguide-coupled devices might provide better signal-to-noise ratios at lower powers because of better rejection of the direct contribution to the transmission.

In order to lower the bistability threshold to build a device that capitalizes on the bistable behaviour, switching to a different cavity geometry should be considered. Nanobeams in particular should provide a higher thermal resistance, as well as potentially allowing for very high optical quality factors[8, 26].

Finally, our observation of this effect shows that linear absorption in silicon can play a significant role in the mid-infrared, and should be taken into account when designing nonlinear devices, e.g. optical amplifiers and wavelength converters[4].

Chapter 4

Gas sensing

4.1 Introduction

A possible application for our photonic crystal cavities is in trace gas sensing. The mid-infrared wavelength region contains absorption bands of many trace gas molecules, corresponding to their vibration modes and associated rotation-vibration bands. Because these bands are very specific to the particular molecule, the mid-infrared is also known as the *fingerprint region*. Detecting small amounts of these trace gases has potential applications for chemical analysis, safety monitoring and in breath analysis for early diagnosis of several diseases[27].

The optical absorption of trace gas molecules is used in several optical detection methods. Current detection methods are usually very bulky. Acquiring high sensitivity requires either multi-pass gas cells to directly measure absorption or using an acoustic resonator[28], relying on photo-acoustic effect for detection. Using an optical cavity can also help boost sensitivity while maintaining a small footprint, either by directly measuring the increased absorption in the cavity through its effect on the spectral features of the cavity, or by indirectly measuring the absorption-induced change in temperature of the gas surrounding an optical cavity. The first method requires the cavity resonance frequency to overlap with one of the absorption lines of the gas. The latter method is called micro-cavity photo-thermal spectroscopy and has the advantage that the detection of the temperature change can be done at a different wavelength range than the gas absorption line, so one can take advantage of the high-Q optical cavities available at e.g. telecom wavelengths[29]. Spectral specificity is provided by using a narrow-band light source to pump the gas near the optical cavity. Both methods have the potential of creating high-sensitivity detection devices which can eventually be integrated on a chip, thus allowing for miniaturization[3].

Using our Quantum Cascade Laser, which has a wavelength range of roughly 4.3–4.6 µm, we can use nitrous oxide (N_2O) to test these detection schemes, since N_2O has a strong absorption band with its peak at 4.47 µm, while almost no other gases show strong absorption in this wavelength region — in fact, the laser range was chosen to fall around the absorption peak of N_2O for this reason. In the laser range, only $^{13}CO_2$ also shows an absorption band, which does not overlap with the N_2O absorption band. While using photothermal detection with

a high-Q cavity in a different wavelength range is an easier way of reaching high detection limits (since high-Q devices are already available), using the direct detection scheme has the advantage of simplicity, since only one light source is needed, and we already have the photonic crystal cavities to test this. Thus, we will test whether detecting N_2O is possible using these cavities.

4.2 Detection limit

Using the simple model from [30], we can estimate the detection limit of our photonic crystal cavities, when it's positioned on one of the absorption peaks. We assume we need $Q_{loss} \approx Q_{cavity}$ so the total Q will be approximately halved, which means the linewidth becomes approximately twice as large. This is a very conservative assumption, so we will obtain a lower bound for the detection limit of our system. The model gives us the equation for Q_{loss}:

$$Q_{loss} = \frac{2\pi n_{gas}}{\alpha \lambda_0 \zeta} \tag{4.1}$$

where n_{gas} is the refractive index of the gas surrounding the cavity, α is the absorption coefficient of the gas in m^{-1}, λ_0 is the resonant wavelength of the cavity in m, and ζ is the portion of the cavity mode that is in the absorbing medium (the gas).

For low concentrations of the trace gas, n_{gas} does not change, so we set it to $n_{air} = 1$. We set λ_0 to the absorption peak of N_2O, which is 4.47e-6 m. From numerical calculations we estimate the portion of the mode that is not in the silicon to be 11 %. Finally, we set $Q_{loss} \approx 15,000$, which results in a minimum detectable absorption coefficient $\alpha = 850$ cm^{-1}. From the HITRAN data we can get the absorption cross section $\kappa = 4.1\text{e-}18$ cm^2/molecule, so the minimum detectable concentration is $\alpha/\kappa = 2.07\text{e}24$ molecules/m^3, which corresponds to a gas mixture with 8.5 % N_2O at atmospheric pressure.

A word of caution is necessary here, since the refractive index of the trace gas shows large changes near its absorption peak according to the Kramers-Kronig relations. At the concentration of 8.5 % the refractive index contribution of the trace gas is no longer negligible and our estimate of the detection limit is either a bit less conservative, or a lot more conservative. The minimum detectable absorption coefficient and thus the concentration are linear in the change in refractive index for a constant detectable Q_{loss}.

The way to improve on this theoretical detection limit is to raise the Q of our cavity, and to pick a cavity design with a larger portion of its optical mode volume in the surrounding gas instead of in the cavity material.

4.3 Experimental

Using our setup, we wish to test the feasibility of the direct detection scheme, where we measure the change in quality factor of the cavity when the gas is present to detect the extra absorption. In order to do this, a gas flow cell was included in the setup (figure 4.1). A flow restrictor and a mass flow controller were used to enable different mixing ratios between two gases, in our case nitrogen and nitrous oxide (N_2O), as shown in the diagram in figure 4.2.

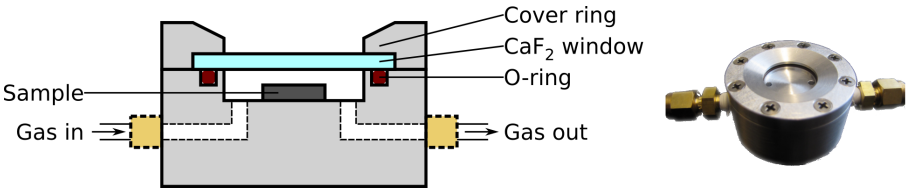

Figure 4.1: (left) Design of the gas flow cell (not to scale). The CaF_2 window is 1 mm thick and the space for the sample is also about 1 mm. An O-ring seals the flow cell. (right) The gas flow cell without sample or window.

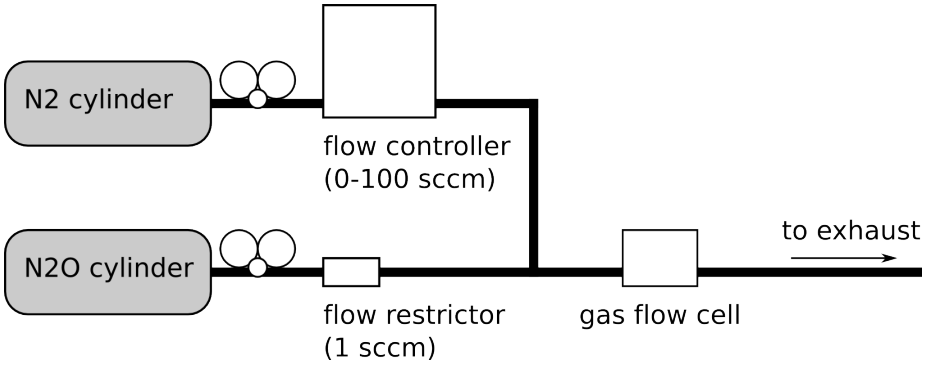

Figure 4.2: Schematic representation of the gas flow control in the setup. A flow restrictor was used for the N_2O flow, while a variable mass flow controller was used to mix in N_2 at different mixing ratios. The gas flow cell was mounted in the optical setup (see figure 4.1).

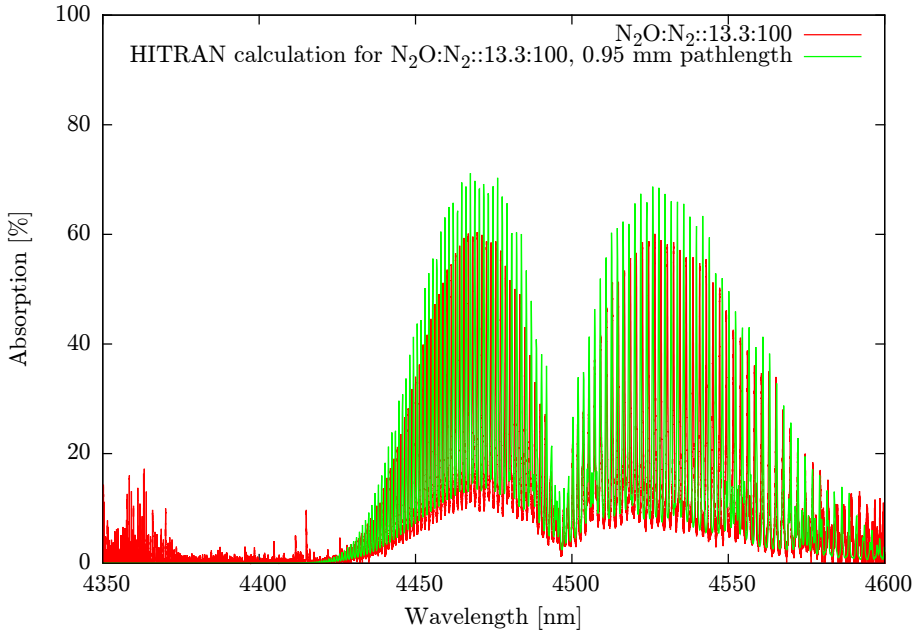

Figure 4.3: N_2O absorption spectrum measured with a gold mirror in the gas flow cell, compared to the result calculated with the HITRAN database for the same concentration and path length.

Our first test of this setup was to flow N_2O gas through the cell with a gold mirror present to directly detect the N_2O absorption spectrum. The result is shown in figure 4.3, together with a calculation of the absorption spectrum from the HITRAN database[31] for the same concentration and path length. The figure shows that the absorption spectrum shows good agreement with the predicted result, confirming that the setup works.

Unfortunately, our preliminary tests did not show any effect of the gas on the spectral features of the cavity. Figure 4.4 shows the spectrum of a high-Q cavity at low power, with the background measurement with N_2O flow to show the location of the absorption peaks of the N_2O. Fitting these spectra yielded Q-factors of around 13,500 in both cases, so no significant change was seen even at almost 12 % N_2O. The reason that the N_2O absorption did not affect the cavity spectrum as much as we estimated could be that the absorption peak was narrower than the cavity spectrum, and the maximum of the absorption peak did not coincide with the cavity resonance. Therefore, the amount of absorption was too low to have an observable effect on the cavity spectrum.

While doing some of the preliminary measurements to test the trace gas sensing, we observed a permanent redshift of the cavity resonance wavelength by at least 5 nm after prolonged laser illumination while flowing pure nitrous oxide over the cavity (figure 4.5). The laser power present was about 22 mW and most of the time the laser was tuned about 10 nm away from the cavity resonance, which was still in the absorption band of the N_2O. The two shifts shown in figure 4.5 occurred after roughly 40 minutes of this exposure. We haven't observed this shift without N_2O present, nor while flowing N_2O without

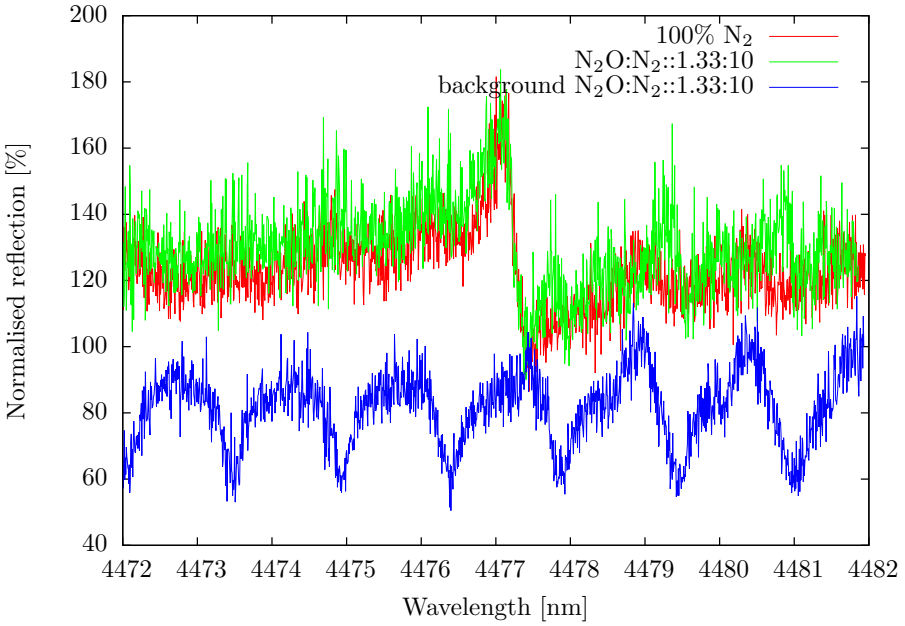

Figure 4.4: Normalised cavity spectrum in a gas flow of 100 % N_2 and in a mixture of N_2O and N_2. The cavity spectra were taken at low power ($<$ 1 mW) and were normalised to the reflection of the unpatterned substrate next to the cavity. This background measurement is shown for the measurement with N_2O (normalised to the pure N_2 background) to show the location of the absorption peaks of the nitrous oxide.

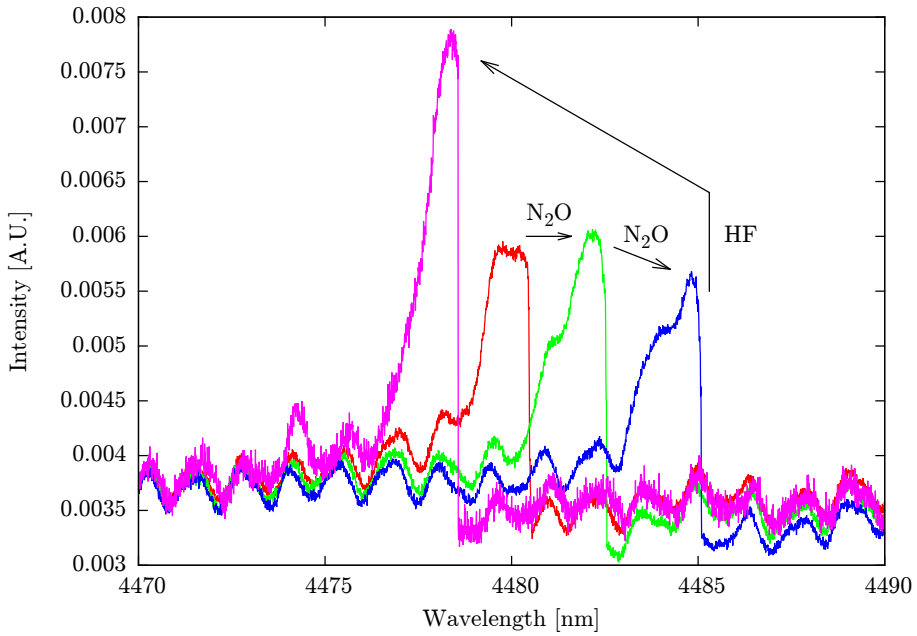

Figure 4.5: Shifting of the resonance frequency of a cavity, as a result of flowing N_2O while illuminating the cavity with about 22 mW of laser radiation for about 40 minutes. Treating the sample with an HF solution undid the redshift and blueshifted the cavity another 2 nm. The spectrum after the HF treatment was taken at a slightly higher input power (∼24 mW). At these high input powers, the shape of the spectrum shows the cavity is bistable.

high-power laser illumination. Also, only the cavity that was illuminated by the laser spot was shifted by this. Finally, when the sample was treated with HF to remove any silicon oxide formed on the cavities, all of the cavities blueshifted by 1 or 2 nm, while the cavity that was redshifted by the N_2O 'treatment' was blueshifted by 8 nm, undoing the previous redshift and ending up about 2 nm blueshifted from its original position. This would indicate we are creating an oxide or nitride layer in the cavity region by flowing N_2O and illuminating it with the laser light[32]. Even though this also alters the quality factor of the cavity, this could prove a tool to tune the cavity resonances to the absorption peaks we are interested in. It also indicates the reverse process, chemical treatment of the surface to remove contaminants or surface roughness, might be succesful in tuning the cavity.

4.4 Conclusion

We introduced a gas cell in our setup to be able to test a gas sensing scheme using the changing spectral properties of our photonic crystal cavities as an indicator of the amount of trace gas present near the cavity. Preliminary tests did not show any change in the spectrum of one of the cavities as a function of the amount of gas present. This is likely the result of the fact that the cavity resonance was not optimally positioned with respect to the absorption spectrum

of the nitrous oxide, and that the absorption peak was narrower than the cavity resonance peak. We did find that flowing nitrous oxide over the cavity under high-powered laser illumination caused the resonance to shift permanently. This shift could be undone by treating the sample with HF, removing any silicon oxides or nitrides present on the cavity. Therefore, we attribute this shift to the growth of oxides and/or nitrides on the silicon in these circumstances.

In order to improve the gas sensing performance of the cavities in this sensing scheme, a number of parameters can be changed. Creating cavities with a higher quality factor and/or a larger portion of the optical mode volume outside of the semiconductor material will make this sensing method more sensitive. Making sure the cavity resonance coincides with an absorption peak of the gas will make sure the optimal sensitivity of the cavity is obtained.

Appendix A

Temporal coupled mode theory

In "Photonic Crystals: Molding the flow of light"[6], a set of equations is derived to describe the stored energy in a cavity based on the coupling constants between the cavity and one or two waveguides or other channels (pp. 198–203). These equations are based on the assumption of weak coupling. Figure A.1 shows an abstract representation of the situation, labeling the variables and constants in the system. A represents the field amplitude in the cavity, normalized in such a way that $|A|^2$ is the electromagnetic energy stored in the cavity. s_{k+} and s_{k-} are the field amplitudes in the incoming and outgoing beam respectively, with k indexing the polarisation. These are normalised in such a way that $|s_{k+}|^2$ and $|s_{k-}|^2$ are the incoming and outgoing power. For this system, the following temporal coupled mode equations hold:

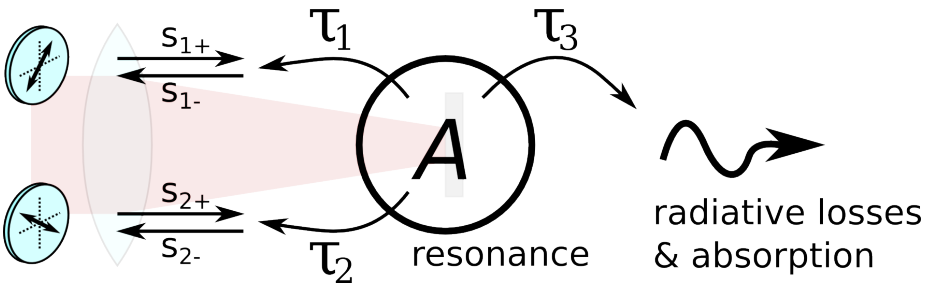

Figure A.1: Schematic representation of the field A in the resonant cavity coupled to a channel carrying the input and output fields s_{k+} and s_{k-}, with k indexing the polarisation of the modes. The cavity is also 'coupled' to a loss channel caused by absorption and radiative losses (emission at the back side of the membrane, and scattering out of the photonic crystal in the plane of the membrane).

$$\frac{dA}{dt} = -i\omega_0 A - \frac{A}{\tau_1} - \frac{A}{\tau_2} - \frac{A}{\tau_3} + \sqrt{\frac{2}{\tau_1}} s_{1+} + \sqrt{\frac{2}{\tau_2}} s_{2+} \tag{A.1}$$

$$s_{1-} = -s_{1+} + \sqrt{\frac{2}{\tau_1}} A \tag{A.2}$$

$$s_{2-} = -s_{2+} + \sqrt{\frac{2}{\tau_2}} A \tag{A.3}$$

ω_0 is the resonance frequency of the cavity. Because of the cross-polarisation in our setup, the input is all in one polarisation, while we detect only the other polarization. This means $|s_{1+}|^2 = P_{in}$ and $|s_{2+}|^2 = 0$, and we are interested in $P_{out} = |s_{2-}|^2$.

If we look at the decay of the stored energy into only 1 channel, e.g. by taking $\tau_2, \tau_3 \to \infty$, while $s_{k+} = 0$, the solution to A.1 takes the form $|A|^2 = |A_0|^2 e^{-2t/\tau_1}$. This means we can identify the quality factor Q_1 with $\omega_0\tau_1/2$. The same argument holds for $\mathrm{Q}_2 = \omega_0\tau_2/2$ and $\mathrm{Q}_3 = \omega_0\tau_3/2$. Because τ_1 and τ_2 describe 2 different polarisation modes in the same physical channel, $\mathrm{Q}_1 = \mathrm{Q}_2 \equiv \mathrm{Q}_c$ describes the coupling of the resonator to the pump and detection channels. Finally, the total energy loss from the cavity is described by $1/\tau_t = 1/\tau_1 + 1/\tau_2 + 1/\tau_3$ and the associated $\mathrm{Q}_t = \omega_0\tau_t/2$.

Now the steady-state solution to A.1 at resonance ($\omega = \omega_0$), averaged over many optical cycles, is:

$$A = \tau_t \sqrt{\frac{2}{\tau_c}} s_{1+} = \frac{2Q_t}{\sqrt{\omega_0 Q_c}} s_{1+} \tag{A.4}$$

$$|A|^2 = \frac{4Q_t^2}{\omega_0 Q_c} |s_{1+}|^2 \tag{A.5}$$

Now writing A.3 in terms of Q_c, squaring it and substituting, we get:

$$|s_{2-}|^2 = \frac{\omega_0}{Q_c} |A|^2 = 4 \left(\frac{Q_t}{Q_c} \right)^2 |s_{1+}|^2 \tag{A.6}$$

In the case where there is no radiative losses or absorption, the power in the detection channel is exactly the power in the input channel, since $1/\mathrm{Q}_t = 1/\mathrm{Q}_1 + 1/\mathrm{Q}_2 + 1/\mathrm{Q}_3 = 2/\mathrm{Q}_c + 1/\mathrm{Q}_3$, so $\mathrm{Q}_t/\mathrm{Q}_c = 1/2$ if $\mathrm{Q}_3 \to \infty$.

Appendix B

Nonlinear resonance shift

We use simple perturbation theory to estimate the relative contributions of the Kerr effect and thermal dispersion due to linear absorption in the silicon membrane. We follow the analysis of ref. [22] to get the equations for the normalized modal refractive index change:

$$\left(\frac{\Delta n}{n}\right)_{kerr} = \frac{\Gamma_{kerr}}{n}\left(\frac{n_2'|A|^2}{V_{kerr}}\right) \tag{B.1}$$

$$\left(\frac{\Delta n}{n}\right)_{thermal} = \frac{\Gamma_{thermal}}{n}\left(\frac{dn}{dT}\frac{dT}{dP_{abs}}P_{abs}\right) \tag{B.2}$$

where Γ_{kerr} and $\Gamma_{thermal}$ are the modal confinement parameters that describe the ratio of the modal field profile that is located in the semiconductor material, n is the refractive index of silicon, $n_2' = (c/n) * n_2$ with n_2 the Kerr coefficient, $|A|^2$ the stored energy in the cavity, calculated in the same way as in appendix A, V_{kerr} the modal volume for the Kerr effect, T the effective temperature of the silicon in the cavity region, and P_{abs} the absorbed power, which we estimated as follows:

$$P_{abs} = \frac{4Q_t^2}{Q_c Q_{abs}}P_{in} \tag{B.3}$$

where Q_t and Q_c represent the total quality factor and the quality factor due to the coupling to the input power P_{in}, as before, and Q_{abs} represents the quality factor due to (linear) absorption in the silicon. Table B.1 shows the values used for the constant parameters in these equations.

The value for n_2 at these wavelengths is extrapolated from published data up to about 2.5 µm, since data at higher wavelengths in the mid-infrared region is not available. The Q_{abs} is an approximation based on impurity levels of the SOI wafers we used, as given by the manufacturer, and free-carrier absorption levels as given in the referenced publication. A better way to estimate this number would be to use the fitting procedure given in ref. [22], however for a rough estimate this should be fine.

Substituting the values given in table B.1 into equations B.1 and B.2 shows that the thermal contribution is roughly 20 times larger than the Kerr effect contribution. Given that equation B.1 is linear in n_2, this parameter would

Table B.1: Parameters used in the model

Parameter	Value	Units	Source
n	3.425	–	[25]
Γ_{kerr}	0.998	–	FDTD
$\Gamma_{thermal}$	0.9335	–	FDTD
V_{kerr}	6.670×10^{-18}	m^3	FDTD
n_2	11×10^{18}	m^2/W	[12, 33]
dn/dT	1.70×10^{-4}	K^{-1}	[34]
dT/dP_{abs}	9.0×10^3	K/W	COMSOL
Q_t	13,600	–	Section 2.4
Q_c	220,000	–	Section 3.3
Q_{abs}	1.75×10^5	–	[35]

have to become a lot larger at longer wavelengths for the Kerr effect to have a significant contribution.

As a last check, we calculated the wavelength shift according to this simple model and compared it to the measured wavelength shift. This results in shifts that are a factor 2 smaller than the experimental data would suggest, which indicates this model has at least some merit, even if it is not quantitatively accurate.

Bibliography

[1] R. Shankar, R. Leijssen, I. Bulu, and M. Lončar, "Mid-infrared photonic crystal cavities in silicon," *Optics Express*, vol. 19, p. 5579, Mar. 2011.

[2] P. Corrigan, R. Martini, E. a. Whittaker, and C. Bethea, "Quantum cascade lasers and the Kruse model in free space optical communication.," *Optics express*, vol. 17, pp. 4355–9, Mar. 2009.

[3] S.-S. Kim, C. Young, and B. Mizaikoff, "Miniaturized mid-infrared sensor technologies.," *Analytical and bioanalytical chemistry*, vol. 390, pp. 231–7, Jan. 2008.

[4] B. Jalali, "Silicon photonics: Nonlinear optics in the mid-infrared," *Nature Photonics*, vol. 4, pp. 506–508, Aug. 2010.

[5] R. Soref, "Mid-infrared photonics in silicon and germanium," *Nature Photonics*, vol. 4, pp. 495–497, Aug. 2010.

[6] J. D. Joannopoulos, *Photonic crystals: molding the flow of light*. Princeton University Press, 2008.

[7] Y. Akahane, T. Asano, B.-s. Song, and S. Noda, "High-Q photonic nanocavity in a two-dimensional photonic crystal.," *Nature*, vol. 425, pp. 944–7, Oct. 2003.

[8] P. B. Deotare, M. W. McCutcheon, I. W. Frank, M. Khan, and M. Lončar, "High quality factor photonic crystal nanobeam cavities," *Applied Physics Letters*, vol. 94, no. 12, p. 121106, 2009.

[9] M. W. McCutcheon, G. W. Rieger, I. W. Cheung, J. F. Young, D. Dalacu, S. Frédérick, P. J. Poole, G. C. Aers, and R. L. Williams, "Resonant scattering and second-harmonic spectroscopy of planar photonic crystal microcavities," *Applied Physics Letters*, vol. 87, no. 22, p. 221110, 2005.

[10] C. Tsay, E. Mujagić, C. K. Madsen, C. F. Gmachl, and C. B. Arnold, "Mid-infrared characterization of solution-processed As_2S_3 chalcogenide glass waveguides," *Optics Express*, vol. 18, p. 15523, July 2010.

[11] R. Soref, S. J. Emelett, and W. R. Buchwald, "Silicon waveguided components for the long-wave infrared region," *Journal of Optics A: Pure and Applied Optics*, vol. 8, pp. 840–848, Oct. 2006.

[12] S. Zlatanovic, J. S. Park, S. Moro, J. M. C. Boggio, I. B. Divliansky, N. Alic, S. Mookherjea, and S. Radic, "Mid-infrared wavelength conversion in silicon waveguides using ultracompact telecom-band-derived pump source," *Nature Photonics*, vol. 4, pp. 561–564, May 2010.

[13] V. Raghunathan, D. Borlaug, R. R. Rice, and B. Jalali, "Demonstration of a Mid-infrared silicon Raman amplifier," *Optics Express*, vol. 15, no. 22, p. 14355, 2007.

[14] X. Liu, R. M. Osgood, Y. A. Vlasov, and W. M. J. Green, "Mid-infrared optical parametric amplifier using silicon nanophotonic waveguides," *Nature Photonics*, vol. 4, pp. 557–560, May 2010.

[15] T. Baehr-Jones, A. Spott, R. Ilic, A. Spott, B. Penkov, W. Asher, and M. Hochberg, "Silicon-on-sapphire integrated waveguides for the mid-infrared.," *Optics express*, vol. 18, pp. 12127–35, June 2010.

[16] A. Spott, Y. Liu, T. Baehr-Jones, R. Ilic, and M. Hochberg, "Silicon waveguides and ring resonators at 5.5 μm," *Applied Physics Letters*, vol. 97, no. 21, p. 213501, 2010.

[17] M. Galli, S. L. Portalupi, M. Belotti, L. C. Andreani, L. O'Faolain, and T. F. Krauss, "Light scattering and Fano resonances in high-Q photonic crystal nanocavities," *Applied Physics Letters*, vol. 94, no. 7, p. 071101, 2009.

[18] M. Notomi, A. Shinya, S. Mitsugi, G. Kira, E. Kuramochi, and T. Tanabe, "Optical bistable switching action of Si high-Q photonic-crystal nanocavities," *Optics Express*, vol. 13, no. 7, p. 2678, 2005.

[19] T. M. Babinec, B. J. M. Hausmann, M. Khan, Y. Zhang, J. R. Maze, P. R. Hemmer, and M. Lončar, "A diamond nanowire single-photon source.," *Nature nanotechnology*, vol. 5, pp. 195–9, Mar. 2010.

[20] M. Soljacić and J. D. Joannopoulos, "Enhancement of nonlinear effects using photonic crystals.," *Nature materials*, vol. 3, pp. 211–9, Apr. 2004.

[21] T. Uesugi, B.-S. Song, T. Asano, and S. Noda, "Investigation of optical nonlinearities in an ultra-high-Q Si nanocavity in a two-dimensional photonic crystal slab.," *Optics express*, vol. 14, pp. 377–86, Jan. 2006.

[22] P. E. Barclay, K. Srinivasan, and O. Painter, "Nonlinear response of silicon photonic crystal microresonators excited via an integrated waveguide and fiber taper.," *Optics express*, vol. 13, pp. 801–20, Mar. 2005.

[23] R. C. Miller, "Optical Second Harmonic Generation in Piezoelectric Crystals," *Applied Physics Letters*, vol. 5, no. 1, p. 17, 1964.

[24] Y. R. Shren, "Miller's coefficient," in *Principles of Nonlinear Optics*, pp. 37–38, Wiley-Interscience, 1st ed., 1984.

[25] D. Chandler-Horowitz and P. M. Amirtharaj, "High-accuracy, midinfrared (450–4000 cm-1) refractive index values of silicon," *Journal of Applied Physics*, vol. 97, no. 12, p. 123526, 2005.

[26] L.-D. Haret, T. Tanabe, E. Kuramochi, and M. Notomi, "Extremely low power optical bistability in silicon demonstrated using 1D photonic crystal nanocavity.," *Optics express*, vol. 17, pp. 21108–17, Nov. 2009.

[27] S.-S. Kim, C. Young, B. Vidakovic, S. G. A. Gabram-Mendola, C. W. Bayer, and B. Mizaikoff, "Potential and Challenges for Mid-Infrared Sensors in Breath Diagnostics," *IEEE Sensors Journal*, vol. 10, pp. 145–158, Jan. 2010.

[28] A. Elia, P. M. Lugarà, C. Di Franco, and V. Spagnolo, "Photoacoustic Techniques for Trace Gas Sensing Based on Semiconductor Laser Sources," *Sensors*, vol. 9, pp. 9616–9628, Dec. 2009.

[29] J. Hu, "Ultra-sensitive chemical vapor detection using micro-cavity photothermal spectroscopy.," *Optics express*, vol. 18, pp. 22174–86, Oct. 2010.

[30] T. Xu, M. S. Wheeler, H. E. Ruda, M. Mojahedi, and J. S. Aitchison, "The influence of material absorption on the quality factor of photonic crystal cavities," *Optics Express*, vol. 17, no. 10, pp. 8343–8348, 2009.

[31] L. Rothman, I. Gordon, A. Barbe, D. Benner, P. Bernath, M. Birk, V. Boudon, L. Brown, A. Campargue, and J.-P. Champion, "The HITRAN 2008 molecular spectroscopic database," *Journal of Quantitative Spectroscopy and Radiative Transfer*, vol. 110, pp. 533–572, June 2009.

[32] a. Gupta, S. Toby, E. Gusev, H. Lu, Y. Li, M. Green, T. Gustafsson, and E. Garfunkel, "Nitrous oxide gas phase chemistry during silicon oxynitride film growth," *Progress in Surface Science*, vol. 59, pp. 103–115, Sept. 1998.

[33] A. D. Bristow, N. Rotenberg, and H. M. van Driel, "Two-photon absorption and Kerr coefficients of silicon for 850–2200 nm," *Applied Physics Letters*, vol. 90, no. 19, p. 191104, 2007.

[34] B. J. Frey, "Temperature-dependent refractive index of silicon and germanium," *Proceedings of SPIE*, pp. 62732J–62732J–10, 2006.

[35] H. Hara and Y. Nishi, "Free Carrier Absorption in p -Type Silicon," *Journal of the Physical Society of Japan*, vol. 21, pp. 1222–1222, June 1966.